Spatial multiomic profiling reveals distinct fibrotic epithelial niches in idiopathic pulmonary fibrosis

Bin Liu[1], Konain Bhatti[1], Iain D. Stewart[1], James May[1], Maria Concetta Zarcone[1], Nathalie Lambie[2], Nik Matthews[2], Rachel L Clifford[3], Charlotte H. Dean[4], Peter M. George[1,9], Richard Hewitt[1,9,10], Elena Lopez-Jimenez[1], Maddy Parsons[11], Simon R Johnson[3], Anna K. Reed[5,6], Elisabetta A. Renzoni[1,9], Jody Rosenblatt[11-13], Amanda L. Tatler[3], Isabel Uwagboe[11], Louise V Wain[7,8], Athol U. Wells[1,9], R. Gisli Jenkins[1], Alison E. John[1]

1. Imperial NIHR Biomedical Research Centre, MTW Centre for Fibrosing Lung Diseases, National Heart and Lung Institute, Imperial College London, United Kingdom

2. NIHR Imperial BRC Genomics Facility, Imperial College London, United Kingdom

3. Centre for Respiratory Research, Translational Medical Sciences, School of Medicine, Biodiscovery Institute, University of Nottingham, United Kingdom

4. National Heart and Lung Institute, Imperial College London, United Kingdom

5. Department of Lung Transplantation, Harefield Hospital. Guys and St Thomas' NHS Foundation Trust, United Kingdom

6. Department of Infectious Diseases, Imperial College London. United Kingdom

7. Department of Population Health Sciences, University of Leicester, United Kingdom

8. National Institute for Health Research Leicester Biomedical Research Centre, United Kingdom

9. Interstitial Lung Disease Unit, Royal Brompton Hospital, Guy's and St Thomas' National Health Service Foundation Trust, United Kingdom

10. King's Centre for Lung Health, School of Immunology and Microbial Sciences, Faculty of Life Science and Medicine, King's College London, United Kingdom

11. Randall Centre for Cell and Molecular Biophysics, King's College London, United Kingdom

12. School of Cancer and Pharmaceutical Sciences, King's College London, London, UK

13. Francis Crick Institute, London, UK

Correspondence to R Gisli Jenkins:
Margaret Turner Warwick Centre for Fibrosing Lung Disease,
National Heart and Lung Institute, Imperial College London, Guy Scadding Building,
Cale Street, London, SW3 6LY
gisli.jenkins@imperial.ac.uk, Tel: +44 (0) 207 594 1063

Conflict of Interest

R.G.J. reports honoraria from Boehringer Ingelheim, Chiesi, Roche, PatientMPower, AstraZeneca, GSK, and consulting fees from AbbVie, AdALta, Apollo Therapeutics, Brainomix, Bristol Myers Squibb, Chiesi, Cohbar, GlaxoSmithKline Pliant, RedX. A.E.J is founder and shareholder of Alevin Therapeutics. I.D.S reports honoraria from patientMpower and is sole director and statistical consultancy of IndigoSigma Insights Ltd. R.H. reports consulting and speaker fees from Boehringer Ingelheim. S.R.J declares personal travel awards from Ferrer. P.M.G. reports honoraria and personal fees from Boehringer Ingelheim, Roche, AstraZeneca, Daiichi-Sankyo, GSK, Avalyn, Brainomix and stock options in Brainomix. L.V.W. claims consultancy fees from Galapagos, Boehringer Ingelheim and GSK. B.L., K.B., J.M., M.C.Z., E.L.-J., A.L.T., R.L.C., C.H.D., N.L., M.P., N.M., A.K.R., E.A.R., J.R., I.U., and A.U.W. declare no competing interests.

Sources of supports

This study was funded by a Medical Research Council Programme Grant (MR/V00235X/1) to R.G.J and MRC Multi-modal grant (MR/W031469/1) awarded to R.G.J, A.E.J, I.D.S., C.D., M.P. and J.R.. RGJ was funded by an NIHR Research Professorship (RP-2017-08-ST2-014). B.L. is a research fellow funded by Action for pulmonary fibrosis. I.D.S. is an advanced research fellow funded by Rayne Foundation. Infrastructure support for this research was provided by the NIHR Imperial Biomedical Research Centre (BRC). The authors acknowledge the Nottingham Biomedical Research Centre (BRC) and Clinical Research Facility (CRF) Respiratory Biobank, Royal Brompton Hospital for their collection of tissue and facilitation of sample transfer. The authors also thank Prof. Paul Matthews, Vicky Chau, and Dorcas Cheung for their technical support in the application of Hyperion imaging mass cytometry.

Author contributions

B.L., K.B., I.D.S., J.M., M.C.Z., I.U., and E.L.-J. contributed to tissue sample collection, in vitro experiments, and data analysis. S.R.J., A.L.T., and R.L.C. provided critical scientific input and supplied human lung tissues. B.L., N.L., and N.M. conducted CosMx sample preparation, processing, and data acquisition. M.P., J.R., R.H., L.V.W., A.K.R., E.A.R., P.M.G., P.L.M., C.D., and A.U.W. critically reviewed and revised the manuscript. B.L., A.E.J., and R.G.J. conceptualized the study and drafted the manuscript, with K.B. contributing to manuscript preparation. A.E.J. and R.G.J. supervised the project, coordinated collaborations, and finalised the manuscript. All authors reviewed and approved the final version of the manuscript.

3.11 Pulmonary Fibrosis/Fibroblast Biology

This article has an online data supplement, which is accessible from this issue's table of content online at www.atsjournals.

Manuscript word count: 3487

Abstract

Background: Idiopathic pulmonary fibrosis (IPF) is a progressive, fatal disease characterised by excessive extracellular matrix deposition within the lung. Recent advances in single-cell RNA sequencing have identified distinct fibrotic populations, yet their origins and spatial relationships remain incompletely understood.

Methods: Using spatial transcriptomics and Hyperion imaging mass cytometry we compared the cellular composition in formalin fixed paraffin embedded fibrotic lesions (n=9 patients) with control lung (n=9), and cellular interactions were inferred using CellChat V2 ligand-receptor analysis. Monolayers of airway epithelial cells were used to identify changes in keratin (KRT) expression following cell detachment and cyclical mechanical stretch.

Results: Spatial multiomics profiling of human lung cells confirmed the *in situ* localisation of previously described IPF-enriched populations, and identified a previously unrecognized $KRT5^{low}/KRT17^{+}$ epithelial population derived from airway basal cells that progressively acquiring molecular features of aberrant basaloid cells, forming a unique fibrotic niche enriched with the Secreted Phosphoprotein 1 (SPP1) positive macrophages. Functional studies demonstrated that epithelial detachment and cyclical mechanical stretch drive KRT5 reduction, providing a mechanism for the emergence of this transitional state. In addition, we also identified distinct immune–stromal niches enriched in lymphocytes and alveolar fibroblasts.

Conclusion: These findings delineate distinct fibrotic epithelial niches in IPF and support a model in which epithelial loss induces aberrant basaloid differentiation and fibroblast activation, with subsequent airway traction and epithelial detachment generating a secondary niche enriched in basal-derived $KRT5^{low}$/KRT17 cells and $SPP1^{+}$ macrophages.

Word count: 232 words

Introduction

Idiopathic pulmonary fibrosis (IPF) is a chronic, progressive, and fatal interstitial lung disease characterized by matrix deposition within the lung which leads to a relentless decline in pulmonary function. IPF is more common with increasing age, and incidence rates are rising with an estimated 1-13 cases per 100,000 population globally(1). IPF is due to the accumulation of environmental risk factors in people with a genetic predisposition. Despite advances in understanding of pathogenesis and improved treatment options, IPF remains a condition with high morbidity and mortality with median survival rates from 3 to 5 years after diagnosis(2, 3).

Recent advances in single-cell sequencing have accelerated understanding of the diverse cellular populations contributing to IPF pathogenesis. A distinct population of Keratin 5 negative ($KRT5^-$) but Keratin 17 positive ($KRT17^+$) epithelial cells has been identified in fibrotic regions of the lung. These $KRT5^-/KRT17^+$ cells also express markers such as Vimentin, matrix metalloproteinase (MMP7), tumour protein p63 (TP63), and SRY-box2 (SOX2), indicating their progenitor-like nature(4-7). Similarly, a unique population of collagen-producing fibroblasts characterized by increased production of type 1 collagen and the expression of collagen triple helix repeat containing 1 (CTHRC1+) have been identified(8, 9). Finally, macrophages that express Secreted Phosphoprotein 1 expressing macrophages (SPP1+)(10) and secrete osteopontin which promotes extracellular matrix production and trigger myofibroblasts activation(11), have been detected.

Spatial multi-omics provide powerful tools for understanding cellular heterogeneity by combining high-dimensional molecular profiling with spatial context. Spatial transcriptomics permits gene expression mapping within intact tissue sections by revealing the spatial distribution of mRNA transcripts, helping to elucidate cellular interactions and microenvironmental influences(12, 13). Furthermore, high-multiplex tissue imaging enables the simultaneous imaging of multiple proteins at the single-cell level *in situ*, providing further detailed information about cellular phenotypes and states while preserving spatial information(14). Combining both technologies enables a deep molecular phenotyping of the cellular heterogeneity in IPF and how these cells interact to contribute to the fibrotic niche.

130 In this study, spatial transcriptomics was combined with Hyperion imaging mass cytometry to
131 comprehensively assess the fibrotic niche within human lung tissue obtained from patients
132 with IPF. We observed a profound reduction in AT1 cells in fibrotic lung, along with an increase
133 in both $KRT5^{+}/KRT17^{+}$ basal, $KRT5^{-}/KRT17^{+}$ aberrant basaloid cells and notably, a hitherto
134 undescribed $KRT5^{low}/KRT17^{+}$ transitional basal cell population. The $KRT5^{low}/KRT17^{+}$ cells
135 communicates primarily with SPP1+ macrophages, yet share gene expression signature with
136 AT2-derived aberrant basaloid cells, which predominantly interact with activated
137 myofibroblasts. In vitro analysis of airway basal epithelial cells revealed that monolayer
138 detachment and cyclical stretch leads to loss of KRT5. These data highlight a novel and
139 important pathway where airway derived progenitor cells contribute to aberrant alveolar
140 repair in IPF, promoting a unique airway derived fibrotic niche.

141 **Materials and Methods:**

142 **Human tissue collection and tissue microarray construction**

143 IPF lung tissues were sourced from the Nottingham NIHR Biomedical Research Centre under
144 ethical approval (REC 08/H0407/1). Non-IPF tissues were collected from Clinical Research
145 Facility (CRF), Royal Brompton Hospital under the ethical approval (NRES 20/SC/0142). Lung
146 tissues were formalin-fixed and paraffin-embedded prior to tissue microarray (TMA)
147 construction. 1 mm cores were sampled from IPF (4 cores) and control (2 cores) tissues.

148 **CosMx SMI data processing and analysis**

149 Machine learning-driven single cell segmentation was performed using AtoMx Spatial
150 Informatics Platform (SIP)(15, 16). For data quality control (QC), cells with negative probe
151 greater than 0.5 and or features less than 20 were filtered out. In total, 180,067 cells were
152 profiled, and raw counts of all cells were exported as a Seurat object from AtoMx SIP for
153 downstream analysis. Total counts normalization was applied. Following normalization,
154 principal component analysis (PCA) and then Uniform Manifold Approximation and Projection
155 (UMAP) and t-distributed Stochastic Neighbor Embedding (tSNE) were performed for
156 dimension reduction and visualisation using Seurat v5(17).

157 **Cell type annotation**

158 We applied a hierarchical stratergy for cell type annotation, starting with Leiden clustering and
159 aggregating clusters into the main cell lineages based on Human Lung Cell Atlas (HLCA) v2(18)
160 level1 markers which are included in the CosMx 1000-plex gene panel: Immune markers:
161 (CD53, PTPRC, COTL1, CXCR4, FCER1G, SRGN, CD52); Epithelial markers: (KRT7, PIGR, KRT8,
162 KRT19, TSPAN8, CSTD2, CXCL17); Endothelial markers: (PECAM1, VWF, RAMP2, IGFBP7,
163 CLEC14A); and Stromal markers: (TPM2, DCN, MGP, CALD1, LUM, TAGLN, COL1A1). These four
164 lineage subsets were then used for downstream cell subtype annotation using the Insitutype
165 algorithm(19), applying semi-supervised cell typing.

166 **Inference of inter-niche and inter-cell communication using CellChat V2**

167 For inference of cell communication, we first constructed a Niche assay from CosMx spatial
168 transcriptomics data by aggregating local cell-type composition and grouping similar
169 neighbourhoods into recurrent niches. Clustering of neighbourhoods revealed seven distinct
170 niches (N1–N7). N1: MyoFB niche, N2: Airway niche,N3: KRT5-/KRT17+ niche,N4: Immune
171 niche,N5: Vascular niche,N6: Alveolar niche, N7: SPP1+ macrophage niche. CellChat V2(20)
172 was used to infer spatially proximal inter-niche communication and intra-niche intercellular
173 communication. CellChat DB V2 was used as the ligand-receptor (L-R) interaction database. A
174 total of 358 L-R pairs were extracted from the NanoString 1000-plex RNA probes panel and
175 used for further analysis.

176 **Hyperion IMC data processing and analysis**

177 Preprocessing, segmentation, and feature extraction of multi-channel Hyperion IMC images
178 were achieved using the IMC Segmentation Pipeline, as previously described(21). Image based
179 single cell spatial analysis of the IMC data was performed using imcRtools and cytomapper R
180 package.

181 **Imaging Flow Cytometry**

182 Imaging flow cytometry of KRT5 in ihBECs was performed using the ImageStream MK II system.
183 Cells were permeabilised and fixed using eBioscience™ Foxp3 / Transcription Factor Staining
184 Buffer Set (Thermo Fisher Scientific) following the supplier's protocol. Following fixation, cells
185 were stained for KRT5 (2ug/mL) antibody for 30mins at 4° in the dark. Gating and downstream
186 analysis was performed using IDEAS software.

All additional details of the materials and methods section are provided in an online data supplement.

Results

Spatial analysis of control and IPF human lung tissues identifies loss of normal alveolar cells and enriched fibrotic cellular populations.

A tissue microarray constructed from nine IPF patients and nine controls were assessed by spatial transcriptomics, yielding 180,067 cells (141,070 IPF and 38,997 controls), with an average of 110 transcripts per cell analysed. Dimensionality reduction revealed four major cellular compartments corresponding to epithelial, stromal, endothelial, and immune lineages (Figure 1A). Spatial mapping of these transcriptionally defined compartments to tissue sections confirmed expected anatomical localization. (Figure 1B).

To generate high-resolution cell type classification, we applied a semi-supervised annotation approach using the Insitutype algorithm, guided by an expression matrix derived from the publicly available single-cell RNA-seq dataset (GSE227136). This resulted in 34 discrete subtypes that clustered into the four major cell classes based on HLCA v2 level 1 marker gene expression (Figure 1C). Analysis of cell type proportions revealed disease-associated alterations. Specifically, alveolar type 1 and type 2 (AT1 and AT2 cells) cell populations were significantly reduced in IPF, whereas basal ($KRT5^{+}/KR17^{+}$, $KRT5^{low}/KRT17^{+}$), and aberrant basaloid ($KRT5^{-}/KRT17^{+}$) epithelial cells were all substantially expanded (Figure 1D). Within the stromal compartment, a marked increase in alveolar fibroblasts and activated myofibroblasts was observed in IPF compared with controls. In addition, immune populations were also enriched, including monocyte derived and $SPP1^{+}$ macrophages as well as decorin expressing plasma cells (Figure 1D).

To validate the findings from transcriptomic data, we applied multiplex imaging mass cytometry on adjacent sections to assess protein-level changes. Unsupervised clustering following single-cell segmentation revealed 15 distinct cell populations, including IPF-enriched cell populations (Figure E2A, B). Eighteen markers overlapped between CosMx SMI and Hyperion IMC marker panel, and most cells expressed at least one of these shared markers in both datasets (Figure E2C, D). In control tissues, $KRT17^{+}/KRT5^{+}$ basal cells were confined to the airways adjacent to secretory airway epithelial cells ($MUC5B^{+}$) and absent from the

217 alveolar parenchyma where high numbers of cells expressing aquaporin-4 (AQP4)$^{+}$ and
218 surfactant protein C (SFTPC)$^{+}$ were observed (Figure 1E). In contrast, IPF-enriched populations
219 displayed distinct spatial distributions: KRT5^{-}/KRT17^{+} epithelial cells lined fibrotic regions and
220 were positioned near KRT5^{+}/KRT17^{+} basal cells (Figure 1F, G). Additionally, KRT5^{-}/KRT17^{+} cells
221 were observed adjacent to AQP4^{+} AT1 cells and in close proximity to SPP1^{+} macrophages
222 (Figure 1F). Meanwhile, CTHRC1^{+} fibroblasts were primarily located within the fibrotic stroma,
223 exhibiting high levels of collagen I expression (Figure 1G). CD20+ lymphocytes were also
224 present within these matrix-rich fibrotic regions, in proximity to CTHRC1^{+} fibroblasts (Figure
225 1G).

226 **Profiling spatial cellular neighbourhoods reveals distinct fibrotic niches**

227 To investigate spatial interactions and tissue-restricted niches, cell neighbourhood analysis
228 was performed as previously described(17, 21) using the CosMx spatial transcriptomic dataset.
229 Seven niches with distinct cellular compositions were identified in CosMx dataset (Figure 2A).
230 *In situ* projection and quantification of cell centroids revealed that control lungs were
231 dominant by an alveolar niche (N6 consisting mainly of alveolar cells), an airway niche (N2
232 enriched for airway epithelial cells), and a vascular niche (N5, defined by smooth muscle and
233 endothelial cells). In contrast, IPF lungs demonstrated a marked reduction of N6, an expansion
234 of N2, and the emergence of abnormal niches characterised by disease-associated cell
235 populations (Figure2A, C). These included four distinct fibrotic niches: (N1) consisting of
236 activated myofibroblasts-and immune cells; (N3) KRT5-/KRT17+ aberrant basaloid cells ,
237 activated myofibroblasts and alveolar macrophages; (N4) an immune-stromal cell niche driven
238 by lymphocytes and fibroblasts; and (N7) an SPP1+ macrophages predominant niche (N7)
239 (Figure2A-2C). To further explore potential communication between niches, we applied
240 CellChat to infer niche-niche interactions. Circle plots scaled by interaction weight revealed
241 sparse interactions in control tissue, whereas IPF exhibited numerous and stronger
242 interactions, particularly involving N3 and N6 (Figure 2D. Ligand-receptor(LR) pair aggregation
243 based on pathway revealed dominant SPP1, collagen, and FN1 signalling in IPF niches (Figure
244 2E), highlighting LR pairs such as SPP1-CD44 and COL6A-CD44 across multiple fibrotic niches
245 (Figure E3).

246 In parallel, cell community analysis of Hyperion IMC data revealed five niches (Figure 2F),
247 including an alveolar niche enriched for SFTPC+ AT2 and AQP4+ AT1 cells, an airway niche

248 composed primarily of basal (KRT5^{+}/KRT17^{+}) and goblet (MUC5B^{+}) epithelial cells, and a
249 vacular niche dominated by αSMA^{+} cells (Figure 2G). Hyperion IMC further identified two
250 distinct fibrotic niches: the first fibrotic niche predominantly featured SPP1^{+} macrophages,
251 KRT5^{-}/KRT17^{+} epithelial cells, and basal epithelial cells (Figure1E, Figure 2F, 2H), while second
252 fibrotic niche was defined by fibrotic fibroblasts (CTHRC1^{+}/COL1^{+}) in association with CD20+
253 lymphocytes (Figure1G, Figure 2F, 2H).

254 **Distinct origins of fibrotic epithlium contribute to fibrotic niches**

255 To further understand the nature and origin of aberrant epithelial cells, we analysed all
256 epithelial cells separately within fibrotic lung. UMAP visualisation revealed two major
257 epithelial populations corresponding to alveolar and airway lineages, including a previously
258 undescribed KRT5^{low}/KRT17^{+} cell, along with a small convergent population of KRT5^{-}/KRT17^{+}
259 cells (Figure 3A). Trajectory inference suggested that KRT5^{-}/KRT17^{+} cells could arise from AT2
260 cells consistent with prior reports (Figure 3B), but also indicated a possible origin from airway
261 basal cells (Figure 3C). To further resolve the relationship between basal, KRT5^{low}/KRT17^{+} and
262 KRT5^{-}/KRT17^{+} epithelial cells, we examined pseudotime expression dynamics of aberrant
263 basaloid markers. KRT5^{low}/KRT17^{+} cells occupied an intermediate state, with elevated
264 expression of growth differentiation factor 15 (GDF15), matrix metallopeptidase 7 (MMP7),
265 transmembrane 4 L six family member 1 (TM4SF1), SRY-box transcription factor 4 (SOX4),
266 integrin subunit beta 6 (ITGB6), integrin subunit alpha V (ITGAV), and cyclin-dependent kinase
267 inhibitor 1A (CDKN1A) relative to basal cells, but lower than KRT5^{-}/KRT17^{+} cells (Figure3D).
268 Spatial mapping centroids (Figure3G, 3J) of these KRT5^{low}/KRT17^{+} cells revealed enrichment
269 in fibrotic epithelial (PanCK+) regions (Figure3E-3F, 3H-I), often interspersed with AT2 cells and
270 KRT5^{-}/KRT17^{+} cells (Figure 3J). Distance analysis demonstrated co-localisation between AT1,
271 AT2, AT2 transitional and KRT5^{-}/KRT17^{+} cells, in contrast KRT5^{low} /KRT17^{+} co-localised with
272 airway cells. Together, these findings suggest two distinct epithelial origins contributing to
273 fibrotic niches (Figure3K).

274 **Unique epithelial niches orchestrate aberrant cell–cell communication in fibrotic lung**

275 To investigate how the three distinct epithelial populations contribute to the aberrant
276 micronenvironment, we applied CellChat Ligand-Receptor (LR) analysis to infer cell-cell
277 communication within each niche. Niche analysis revealed three unique epithelial associated

niches- N2, an airway niche with cystic airspaces lined by basal cells (“Basal predominant”); N7, an SPP1 macrophage niche enriched for KRT5^{low} basal cells (“Basal.KRT5low predominant”); and N3, the aberrant basaloid niche defined by high level of KRT5^{-}/KRT17^{+} epithelial cells (Figure2A, 4A-C). L-R analysis revealed distinct interaction patterns: “Basal predominant” niches showed active crosstalk among airway epithelial cells, macrophages and vascular endothelial cells (Figure4D); “Basal.KRT5low predominant” niches demonstrated strong interactions between KRT5low basal cells and SPP1+ macrophages (Figure 4E); and aberrant basaloid niches displayed marked interactions with activated myofibroblasts (Figure 4F).

In situ projection of cell centroids onto SPP1 expression maps showed robust overlap of KRT5^{low} basal cell with regions of high SPP1 expression (Figure 4H), compared with basal cell or aberrant basaloid cells (Figure4G, I). Distance measurement confirmed these findings, with KRT5^{low} basal cells showing a sharp peak near zero to SPP1+ macrophages (Figure E4A).

For cross-platform comparison, the KRT5 expression range corresponding to the KRT5^{low} basal population was derived from pseudotime analysis in CosMx data and applied to Hyperion IMC (Figure E4B-C, grey-shaded area), allowing stratification of all KRT17^{+} cells into Basal, KRT5^{low} basal and aberrant basaloid cell populations. Distance analysis revealed a greater proportion of KRT5^{low} epithelial cells localised closer to SPP1^{+} macrophages (Figure E4D), supporting preferential interactions between disease-associated epithelial states and SPP1^{+} macrophages.

To further resolve the potential underlying mechanisms, we specifically examined SPP1-mediated LR pairs across niches. In the basal-predominant (N2) niche , SPP1–(ITGAV+ITGB6) signalling was uniquely restricted to SPP1^{+} macrophages and KRT5^{low} basal cells (Figure E5A). This interaction was further amplified in the basal.KRT5^{low} (N7) predominant niche (Figure E5B), where SPP1^{+} macrophages emerged as the dominant source of SPP1–integrin signaling to KRT5^{low} basal cells. In contrast, the aberrant basaloid niche (N3) displayed a markedly different communication landscape, characterised by broad SPP1-integrin LR pairs, originating from diverse cell types and converging on KRT5^{-}/KRT17^{+} cells (Figure E5C). In addition, the immune–stromal niche (N4), composed of lymphocytes, vascular endothelial cells, and alveolar fibroblasts, was characterised by strong ECM–receptor and chemokine signalling (Figure E6).

308

309 **Basal cell detachment is associated with loss of KRT5 expression highlighting a novel origin**
310 **of fibrotic epithelial cells.**

311 Previous transcriptomic studies have not identified a population of KRT5^{low} cells derived from
312 basal cells, however work by Vanna and colleagues(22) revealed that epithelial cell
313 detachment was closely associated with transcript based niches that associate with KRT5-
314 /KRT17+ cells. Therefore, to understand whether epithelial detachment could lead to loss of
315 KRT5, patterns of KRT5 and KRT17 expression were assessed in overcrowded monolayers of
316 iHBECs and primary basal cells and in the cells which detached from these monolayers.
317 Detached iHBECs showed a dramatic reduction in KRT5 mRNA but retained high levels of
318 *KRT17* mRNA (Figure 5A). Flow imaging cytometry of individual iHBECs confirmed that cells
319 that had been retained in the monolayer had consistently high levels of KRT5 protein which
320 was reduced or absent in iHBECs that had detached from the monolayer (Figure 5B). Similarly,
321 flow cytometric analysis showed expression of KRT5 and KRT17 were both high in iHBEC
322 (Figure 5C) and primary basal cell monolayers (Figure 5D) but there was a distinct population
323 of KRT5^{-} and KRT5^{low} cells in both iHBECs and primary basal cells following detachment (Figure
324 5C and D). Finally to understand if mechanical forces might contribute to the development of
325 the fibrotic epithelial cell phenotype, primary small airway epithial cells were subjected to
326 cyclical mechanical stretch for upt to 24hrs and showed a progressive loss of KRT5 expression
327 while KRT17 remained intact (Figure 5E).

328

329 **Discussion**

330 This study applied bi-level spatial multi-omics to resolve the complex cellular architecture of
331 IPF lung tissue, delineate the spatial organization and interactions of key IPF-associated cell
332 populations, and define distinct fibrotic niches. Our findings confirm and extend single-cell(4,
333 5, 7, 8) and recent spatial transcriptomic studies(22-24) that identified IPF-enriched
334 populations such as KRT5^{-}/KRT17^{+} aberrant basaloid cells, activated myofibroblasts, and
335 SPP1^{+} macrophages and described dysregulated niches characterized by alveolar loss,
336 macrophage reprogramming, and fibroblast activation. Importantly, here we reveal an
337 intermediate KRT5^{low}/KRT17^{+} basal population enriched within fibrotic niches, demonstrating

338 experimentally that epithelial detachment and mechanical stretch result in KRT5 loss, with
339 these cells localized within SPP1^{+} macrophage-enriched fibrotic regions.

340 Consistent with prior murine(7, 25) and human (6, 26) single-cell studies, our trajectory
341 analysis suggests that KRT5^{-}/KRT17^{+} aberrant basaloid cells could arise from AT2 cells and form
342 a fibrotic niche in association with activated myofibroblasts. Intriguingly, our analysis also
343 identified an intermediate transcriptional profile of the KRT5^{low}/KRT17^{+} population between
344 KRT5^{+} basal and KRT5^{-}/KRT17^{+} aberrant basaloid cells. Distance analysis reveals a close but
345 not overlapping spatial location of these KRT5^{low} transitional cells to basal cells, suggesting
346 their origin. In murine models, lineage tracing has demonstrated that KRT5^{+} airway basal cells
347 can migrate into the alveolar region following injury(27, 28), whereas in human lung they have
348 been implicated in IPF pathogenesis through de-differentiation into KRT17^{+} epithelium(29),
349 and aberrant expansion into the distal lung under fibrotic ECM remodeling(30). Our data
350 further support that KRT5^{+} basal cells comprise a substantial fraction of epithelial cells within
351 the fibrotic niche although the role they play in fibrogenesis is not clear. Airway basal cells
352 have been previously identified as self-renewing progenitor cells capable of differentiating
353 into various lung epithelial cells(31-34) following injury, and this observation suggests that
354 KRT5^{+} basal cells may also serve as a source for the KRT17^{+} fibrotic epithelium, supporting the
355 hypothesis that small airways could play a central role in IPF pathogenesis(35). Whether this
356 reflects a primary defect following airway injury, or a secondary response to alveolar injury,
357 collapse and fibrotic contraction leading to traction associated change of the small airways
358 remains unclear. A recent study has also shown that epithelial detachment overlaps with
359 niches enriched for KRT5^{-}/KRT17^{+} aberrant basaloid cells(22). In line with this, our *in vitro* data
360 confirm that detachment, and mechanical forces, can trigger progressive loss of KRT5
361 expression across diverse airway epithelial cells. Taken together, these findings suggest that in
362 the disease state, airway basal cells may transition through a KRT5^{low}/KRT17^{+} intermediate
363 population, acquiring aberrant basaloid transcriptional profile, and contribute to the
364 formation of fibrotic niches.

365 Our identification of three distinct epithelial niches raises the intruiging possibility that loss of
366 both AT1 and AT2 cells may be the initial defect in fibrogenesis. As AT2 cells fail to
367 transdifferentiate appropriately, aberrant basaloid cells accumulate and form a primary
368 fibrotic niche in association with activated myofibroblasts. Progressive matrix deposition and

369 myofibroblast expension within this niche likely alters mechanical force generation around the
370 small airways, driving the emergence of two “secondary fibrotic niches”. The first is a basal
371 cell predominant niche characterised by dilated and expanded airways(30), and the second is
372 a $KRT5^{low}/KRT17^{+}$ niche, marked by detached and stretched epithelium that progressively
373 loses KRT5 in an attempt to compensate for the loss of alveolar epithelial cells. With disease
374 progression, these secondary fibrotic niches expand, as reflected by increasing numbers of
375 both $KRT5^{+}$ basal cells and $KRT5^{-}/KRT17^{+}$ cells in more severe IPF[27]. Notably, niche analysis
376 indicates that $KRT5^{low}/KRT17^{+}$ form a distinct niche in close association with $SPP1^{+}$
377 macrophages raising the interesting possibility that interaction of $SPP1^{+}$ macrophages, either
378 directly or indirectly, with airway basal cells through the SPP1-αvβ6 integrin axis can promote
379 pulmonary fibrosis. However future functional studies are warranted to confirm this potential
380 interaction.

381 In addition our analysis also highlights the emergence of distinct immune–stromal niches in
382 IPF. We observed a subset of lymphocytes preferentially localise within decorin-rich stromal
383 regions, where they interact strongly with vascular endothelial cells and alveolar fibroblasts.
384 Ligand–receptor inference revealed that alveolar fibroblasts signal to plasma cells through
385 CXCL12–ACKR3, and collagen–CD44 pairs, suggesting a matrix-dependent mechanism of
386 plasma cell recruitment and retention. A recent study by Yang et al.(36) demonstrated that
387 CXCL12-expressing fibroblasts promote plasma cell accumulation within tertiary lymphoid
388 structures in IPF, consistent with our observations. These observations highlight dynamic
389 immune–stromal crosstalk in IPF, the functional consequences of which remain to be fully
390 understood.

391 Our study represent one of the largest spatial multi-omics comparisons of IPF and control
392 lungs, with transcriptomic findings validated at the protein level by Hyperion IMC. We also
393 provide proof-of-principle that airway basal cells can lose KRT5 expression under conditions
394 relevant to fibrogenesis. However, our study has some limitations. The nature of spatial
395 transcriptomics limits the number of samples available for analysis and impacts the
396 generalisability of our findings, although the replication of previously described niches is
397 reassuring. Similarly there was incomplete coverage of transcripts for analysis, with CTHRC1
398 being absent from the CosMx SMI, however, replication with Hyperion IMC and the use of
399 alternative markers increase confidence in our findings.

In conclusion, this study identified three distinct fibrotic epithelial niches: a primary fibrotic niche characterised by aberrant basaloid ($KRT5^-/KRT17^+$) cells and activated myofibroblasts; and two secondary fibrotic epithelial niches characterised by airway basal cells or basal cell derived $KRT5^{low}/KRT17^+$ population in close association with $SPP1^+$ macrophages. The enrichment of $KRT5^+$ airway basal cells and abnormal $KRT5^{low}/KRT17^+$ basal cells within distinct niches supports the hypothesis that airway basal cells serve as a major source of fibrotic epithelium. Together with immune–stromal niches that may contribute to fibroblast activation, these findings provide a refined cellular framework for understanding the evolution of progressive fibrotic lung disease.

Reference

1. Maher TM, Bendstrup E, Dron L, Langley J, Smith G, Khalid JM, Patel H, Kreuter M. Global incidence and prevalence of idiopathic pulmonary fibrosis. *Respir Res* 2021; 22: 1-10.
2. Marshall DC, Salciccioli JD, Shea BS, Akuthota P. Trends in mortality from idiopathic pulmonary fibrosis in the European Union: an observational study of the WHO mortality database from 2001–2013. *Eur Respir J* 2018; 51.
3. Ley B, Collard HR, King Jr TE. Clinical course and prediction of survival in idiopathic pulmonary fibrosis. *Am J Respir Crit Care Med* 2011; 183: 431-440.
4. Habermann AC, Gutierrez AJ, Bui LT, Yahn SL, Winters NI, Calvi CL, Peter L, Chung M-I, Taylor CJ, Jetter C. Single-cell RNA sequencing reveals profibrotic roles of distinct epithelial and mesenchymal lineages in pulmonary fibrosis. *Science advances* 2020; 6: eaba1972.
5. Adams TS, Schupp JC, Poli S, Ayaub EA, Neumark N, Ahangari F, Chu SG, Raby BA, DeIuliis G, Januszyk M. Single-cell RNA-seq reveals ectopic and aberrant lung-resident cell populations in idiopathic pulmonary fibrosis. *Science advances* 2020; 6: eaba1983.
6. Heinzelmann K, Hu Q, Hu Y, Dobrinskikh E, Ansari M, Melo-Narváez MC, Ulke HM, Leavitt C, Mirita C, Trudeau T. Single-cell RNA sequencing identifies G-protein coupled receptor 87 as a basal cell marker expressed in distal honeycomb cysts in idiopathic pulmonary fibrosis. *Eur Respir J* 2022; 59.
7. Strunz M, Simon LM, Ansari M, Kathiriya JJ, Angelidis I, Mayr CH, Tsidiridis G, Lange M, Mattner LF, Yee M. Alveolar regeneration through a Krt8+ transitional stem cell state that persists in human lung fibrosis. *Nature communications* 2020; 11: 3559.
8. Tsukui T, Sun K-H, Wetter JB, Wilson-Kanamori JR, Hazelwood LA, Henderson NC, Adams TS, Schupp JC, Poli SD, Rosas IO. Collagen-producing lung cell atlas identifies multiple subsets with distinct localization and relevance to fibrosis. *Nature communications* 2020; 11: 1920.
9. Mayr CH, Sengupta A, Asgharpour S, Ansari M, Pestoni JC, Ogar P, Angelidis I, Liontos A, Rodriguez-Castillo JA, Lang NJ. Sfrp1 inhibits lung fibroblast invasion during transition to injury-induced myofibroblasts. *Eur Respir J* 2024; 63.
10. Morse C, Tabib T, Sembrat J, Buschur KL, Bittar HT, Valenzi E, Jiang Y, Kass DJ, Gibson K, Chen W. Proliferating SPP1/MERTK-expressing macrophages in idiopathic pulmonary fibrosis. *Eur Respir J* 2019; 54.

440 11. Hoeft K, Schaefer GJ, Kim H, Schumacher D, Bleckwehl T, Long Q, Klinkhammer BM, Peisker
441 F, Koch L, Nagai J. Platelet-instructed SPP1+ macrophages drive myofibroblast
442 activation in fibrosis in a CXCL4-dependent manner. *Cell Rep* 2023; 42.
443 12. Rao A, Barkley D, França GS, Yanai I. Exploring tissue architecture using spatial
444 transcriptomics. *Nature* 2021; 596: 211-220.
445 13. Tian L, Chen F, Macosko EZ. The expanding vistas of spatial transcriptomics. *Nat Biotechnol*
446 2023; 41: 773-782.
447 14. de Souza N, Zhao S, Bodenmiller B. Multiplex protein imaging in tumour biology. *Nature*
448 *Reviews Cancer* 2024; 24: 171-191.
449 15. Reeves JW, Henderson D, Crow M, Munn A, Terai K, Schmid J. Solving the problem of spatial
450 informatics: Harnessing the power of the cloud and enabling the integration of open
451 source tools for spatial 'omics analytics. *Cancer Res* 2023; 83: 2083-2083.
452 16. Rosenbloom A, Bonnett S, Conner M, Phan-Everson T, Lewis Z, Ong G, Liang Y, Brown E,
453 Pan L, Wardhani A. A complete pipeline for high-plex spatial proteomic profiling and
454 analysis of neural cell phenotypes on the CosMx™ Spatial Molecular Imager and
455 AtoMx™ Spatial Informatics Platform. *Alzheimer's & Dementia* 2023; 19: e076665.
456 17. Hao Y, Stuart T, Kowalski MH, Choudhary S, Hoffman P, Hartman A, Srivastava A, Molla G,
457 Madad S, Fernandez-Granda C. Dictionary learning for integrative, multimodal and
458 scalable single-cell analysis. *Nat Biotechnol* 2024; 42: 293-304.
459 18. Sikkema L, Ramírez-Suástegui C, Strobl DC, Gillett TE, Zappia L, Madissoon E, Markov NS,
460 Zaragosi L-E, Ji Y, Ansari M. An integrated cell atlas of the lung in health and disease.
461 *Nat Med* 2023; 29: 1563-1577.
462 19. Danaher P, Zhao E, Yang Z, Ross D, Gregory M, Reitz Z, Kim TK, Baxter S, Jackson S, He S.
463 Insitutype: likelihood-based cell typing for single cell spatial transcriptomics. *bioRxiv*
464 2022: 2022.2010. 2019.512902.
465 20. Jin S, Plikus MV, Nie Q. CellChat for systematic analysis of cell–cell communication from
466 single-cell transcriptomics. *Nat Protoc* 2025; 20: 180-219.
467 21. Windhager J, Zanotelli VRT, Schulz D, Meyer L, Daniel M, Bodenmiller B, Eling N. An end-
468 to-end workflow for multiplexed image processing and analysis. *Nat Protoc* 2023; 18:
469 3565-3613.
470 22. Vannan A, Lyu R, Williams AL, Negretti NM, Mee ED, Hirsh J, Hirsh S, Hadad N, Nichols DS,
471 Calvi CL. Spatial transcriptomics identifies molecular niche dysregulation associated
472 with distal lung remodeling in pulmonary fibrosis. *Nat Genet* 2025; 57: 647-658.
473 23. Mayr CH, Santacruz D, Jarosch S, Bleck M, Dalton J, McNabola A, Lempp C, Neubert L, Rath
474 B, Kamp JC. Spatial transcriptomic characterization of pathologic niches in IPF. *Science*
475 *Advances* 2024; 10: eadl5473.
476 24. Franzén L, Olsson Lindvall M, Hühn M, Ptasinski V, Setyo L, Keith BP, Collin A, Oag S,
477 Volckaert T, Borde A. Mapping spatially resolved transcriptomes in human and mouse
478 pulmonary fibrosis. *Nat Genet* 2024: 1-12.
479 25. Choi J, Park J-E, Tsagkogeorga G, Yanagita M, Koo B-K, Han N, Lee J-H. Inflammatory signals
480 induce AT2 cell-derived damage-associated transient progenitors that mediate
481 alveolar regeneration. *Cell stem cell* 2020; 27: 366-382. e367.
482 26. Lang NJ, Gote-Schniering J, Porras-Gonzalez D, Yang L, De Sadeleer LJ, Jentzsch RC, Shitov
483 VA, Zhou S, Ansari M, Agami A. Ex vivo tissue perturbations coupled to single-cell RNA-
484 seq reveal multilineage cell circuit dynamics in human lung fibrogenesis. *Sci Transl Med*
485 2023; 15: eadh0908.

27. Zhao Y, Zhou Y, Zhang W, Liu M, Duan J, Zhang X, Ma Q, Wang Y, Zhang Y, Guo Z. Cloned airway basal progenitor cells to repair fibrotic lung through re-epithelialization. *Nature Communications* 2025; 16: 1303.
28. Zuo W, Zhang T, Wu DZA, Guan SP, Liew A-A, Yamamoto Y, Wang X, Lim SJ, Vincent M, Lessard M. p63+ Krt5+ distal airway stem cells are essential for lung regeneration. *Nature* 2015; 517: 616-620.
29. Jaeger B, Schupp JC, Plappert L, Terwolbeck O, Artysh N, Kayser G, Engelhard P, Adams TS, Zweigerdt R, Kempf H. Airway basal cells show a dedifferentiated KRT17highPhenotype and promote fibrosis in idiopathic pulmonary fibrosis. *Nature communications* 2022; 13: 5637.
30. Hewitt RJ, Puttur F, Gaboriau DC, Fercoq F, Fresquet M, Traves WJ, Yates LL, Walker SA, Molyneaux PL, Kemp SV. Lung extracellular matrix modulates KRT5+ basal cell activity in pulmonary fibrosis. *Nature Communications* 2023; 14: 6039.
31. Rock JR, Onaitis MW, Rawlins EL, Lu Y, Clark CP, Xue Y, Randell SH, Hogan BL. Basal cells as stem cells of the mouse trachea and human airway epithelium. *Proceedings of the National Academy of Sciences* 2009; 106: 12771-12775.
32. Tata PR, Mou H, Pardo-Saganta A, Zhao R, Prabhu M, Law BM, Vinarsky V, Cho JL, Breton S, Sahay A. Dedifferentiation of committed epithelial cells into stem cells in vivo. *Nature* 2013; 503: 218-223.
33. Xi Y, Kim T, Brumwell AN, Driver IH, Wei Y, Tan V, Jackson JR, Xu J, Lee D-K, Gotts JE. Local lung hypoxia determines epithelial fate decisions during alveolar regeneration. *Nat Cell Biol* 2017; 19: 904-914.
34. Carraro G, Mulay A, Yao C, Mizuno T, Konda B, Petrov M, Lafkas D, Arron JR, Hogaboam CM, Chen P. Single-cell reconstruction of human basal cell diversity in normal and idiopathic pulmonary fibrosis lungs. *Am J Respir Crit Care Med* 2020; 202: 1540-1550.
35. Berigei SR, Nandy S, Yamamoto S, Raphaely RA, DeCoursey A, Lee J, Sharma A, Auchincloss HG, Gaissert H, Lanuti M. Microscopic Small Airway Abnormalities Identified in Early Idiopathic Pulmonary Fibrosis In Vivo Using Endobronchial Optical Coherence Tomography. *Am J Respir Crit Care Med* 2024.
36. Yang Z, Cao G, Tan X, Orfanos S, Jude J, Barbet G, An SS, Jiang D, Panettieri Jr RA, Yang Q. Distinct mural cells and fibroblasts promote pathogenic plasma cell accumulation in idiopathic pulmonary fibrosis. *Eur Respir J* 2025; 65.

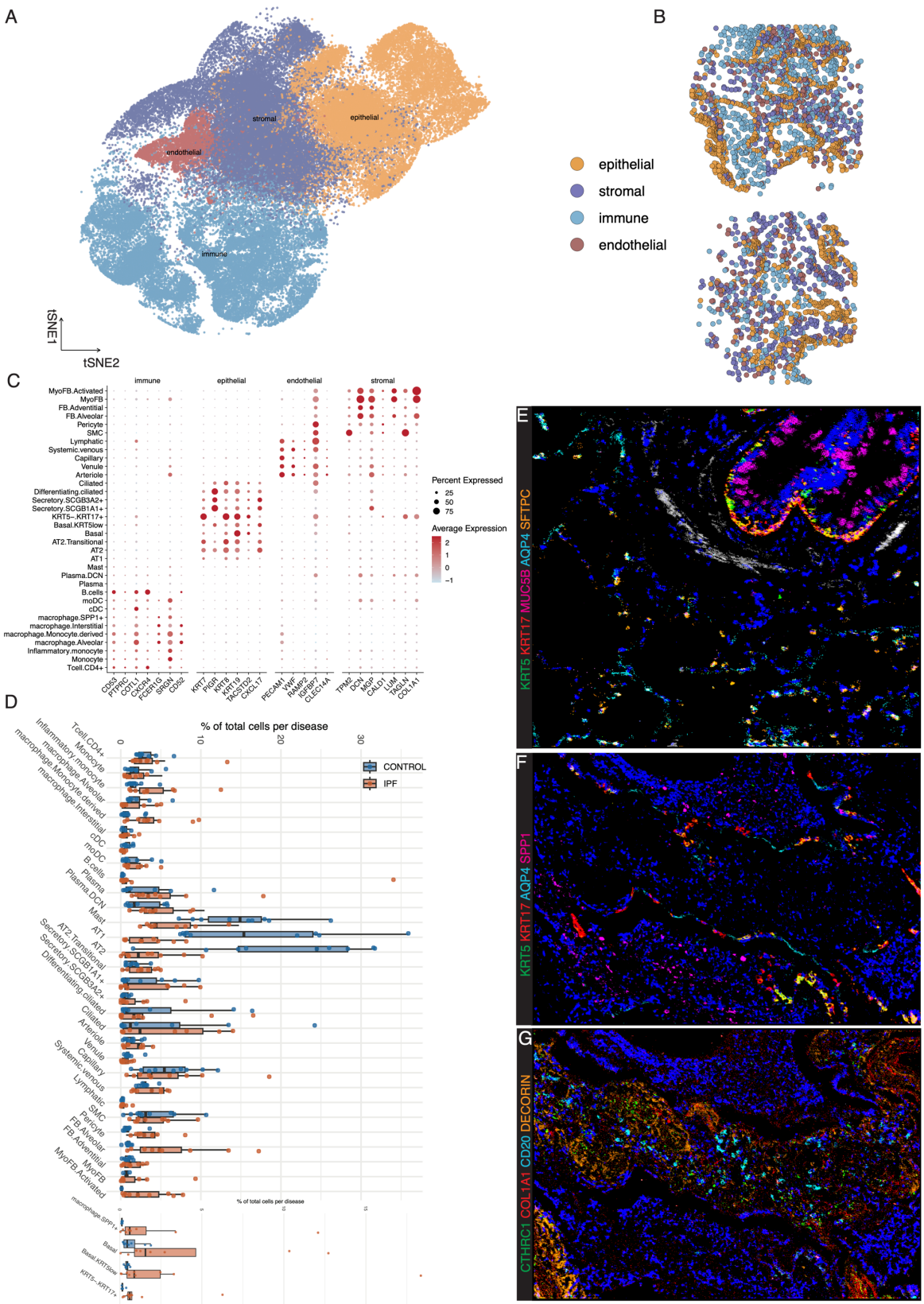

Figure 1. Cellular composition of control and idiopathic pulmonary fibrosis (IPF) lungs profiled by CosMx Spatial Molecular Imaging A t-SNE embedding of all CosMx single-cell

525 transcriptomic profiles, coloured by major lineage (epithelial, immune, endothelial, stromal).
526 B Representative CosMx images showing the spatial distribution of epithelial, immune,
527 endothelial, and stromal lineages in lung tissue sections. C Dot plot showing expression of
528 HLCA v2 level 1 marker genes across the final 34 annotated cell types. Dot size represents the
529 proportion of cells expressing each gene and colour intensity indicates average expression,
530 confirming annotations within epithelial, immune, endothelial, and stromal lineages. D
531 Boxplots showing the proportion of each cell type, expressed as a percentage of total cells per
532 sample, in control (n = 9) and IPF (n = 9) lungs. Points represent individual samples. Boxplots
533 indicate the median, interquartile range (box), and whisker extension. Colours correspond to
534 disease state. E-G representative Hyperion imaging mass cytometry images of E Control lung
535 tissue showing $AQP4^+$/$SFTPC^+$ alveolar parenchyma and $KRT5^+$/$KRT17^+$/$MUC5B^+$ airway
536 epithelium surrounded by αSMA^+ regions. F IPF lung tissue with $KRT5^-$/$KRT17^+$ epithelial cells
537 located in close proximity to KRT5+/$KRT17^+$ basal cells, $AQP4^+$ AT1 cells, and near $SPP1^+$
538 macrophages G IPF lung tissue showing $CD20^+$ B cells positioned near $CTHRC1^+$ fibroblasts
539 within collagen I– and decorin-rich fibrotic region. AT1, alveolar type 1; AT2, alveolar type 2;
540 FB, fibroblast; MyoFB, myofibroblast; SMC, smooth muscle cell; DCN, decorin; moDC,
541 monocyte-derived dendritic cell; cDC, classical dendritic cell; NK, natural killer; Mast, mast cell

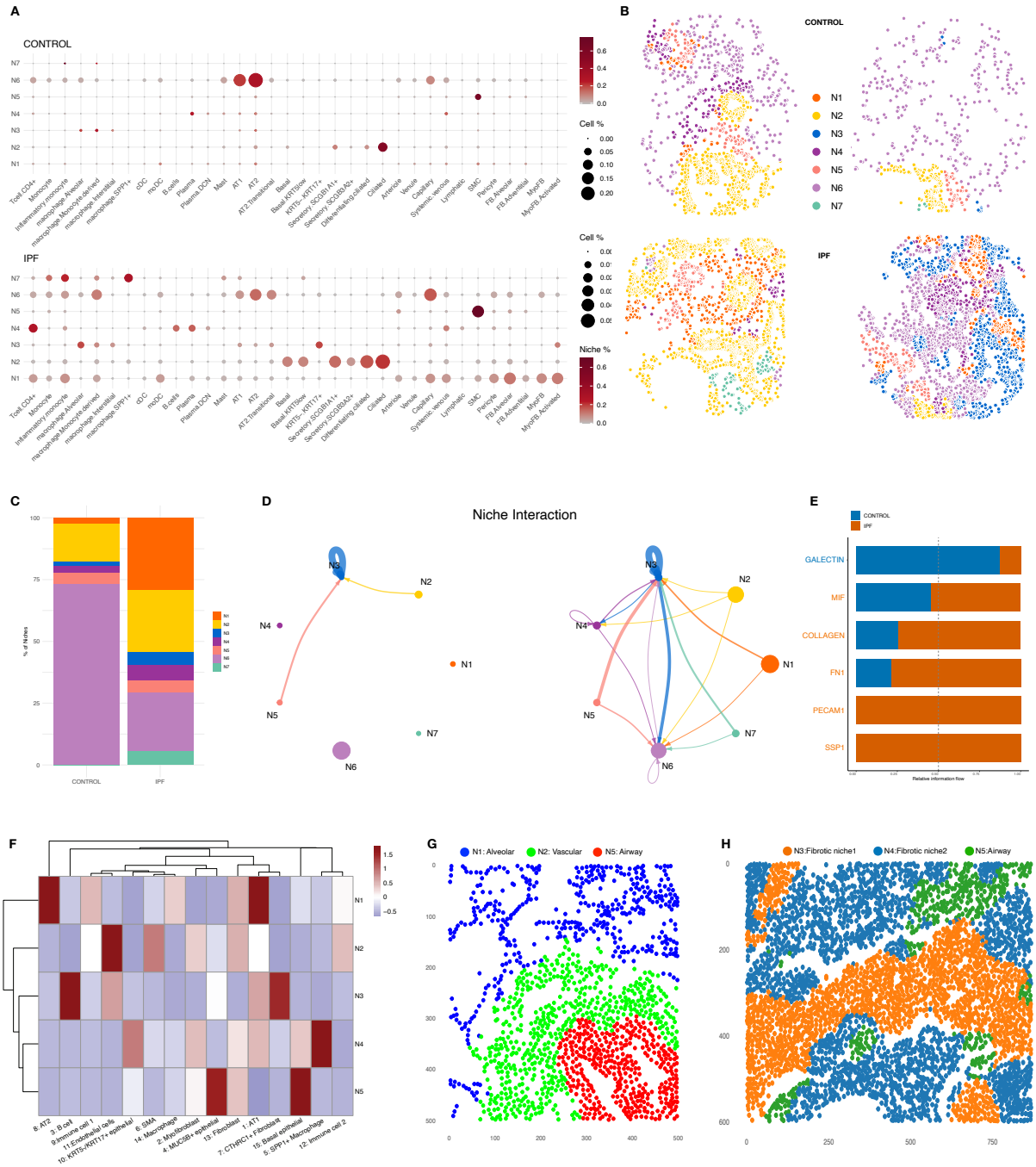

Figure 2. Spatial niche architecture in control and IPF lungs CosMx analysis of spatial niches in control and IPF lungs **(A,B)**. **A** Dot plot showing the cellular composition of niches (N1–N7) in control (top) and IPF (bottom). Dot size represents the proportion of each cell type relative to the total cell number, while dot colour indicates the proportion of each cell type within a given niche. **B** Spatial maps of cell centroids coloured by niche identity (N1–N7) in control (top) and IPF (bottom). N1 active myofibroblast niche, N2 airway niche, N3 KRT5^{-}/KRT17^{+} niche, N4

549 immune niche, N5 vascular niche, N6 alveolar niche, and N7 SPP1^{+} macrophage niche. **C** niche
550 composition of control and IPF tissue shown as a stacked bar plot. Cellchat analysis of inferred
551 ligand–receptor interactions depicting **D** the inter-niche communication in control and IPF
552 lung tissues. Nodes represent cell types and edges indicate predicted interactions, with edge
553 width proportional to interaction strength, and **E** top ranked pathway aggregated by ligand-
554 receptor pairs in control and IPF. Hyperion IMC analysis of spatial niches in control and IPF
555 lungs **(F–H)**. **F** Heatmap showing the cell type composition of niches (N1–N5). Rows
556 correspond to niches and columns to cell types. Colours indicate relative enrichment of each
557 cell type across niches (dark red, enriched; dark blue, depleted; white, average). N1 alveolar
558 niche, N2 vascular niche, N3 fibrotic niche 1, N4 fibrotic niche 2, and N5 airway niche. D, E
559 Representative spatial maps of cell centroids coloured by niche identity (N1–N5) in control **(G)**
560 and IPF **(H)**.

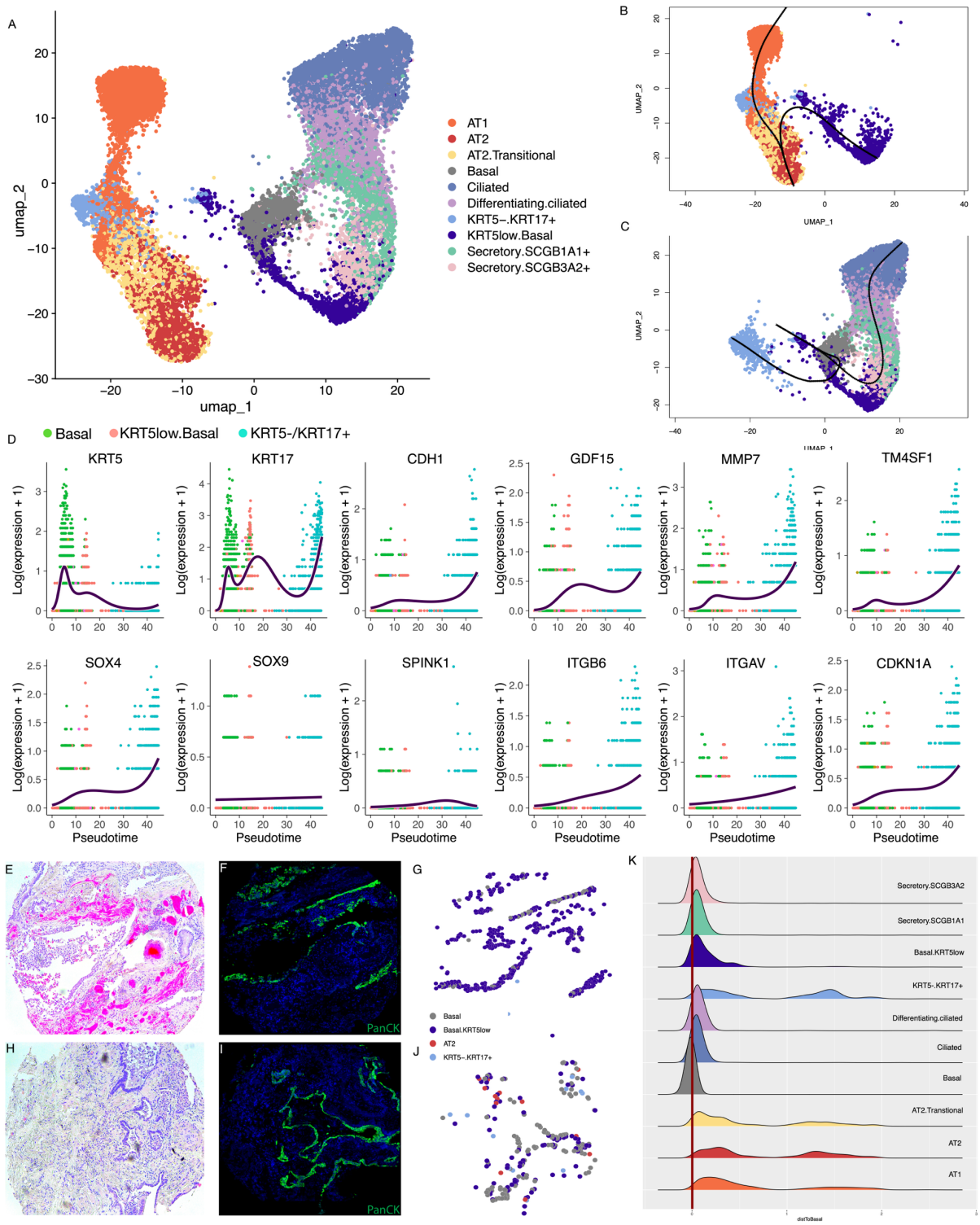

Figure 3. Airway basal cell–derived KRT5^{low}/KRT17^{+} transitional state marks progression toward an aberrant basaloid transcriptional signature A UMAP embedding of epithelial subclusters from control and IPF lungs. **B-C** Mapping of KRT5low basal and KRT5^{-}/KRT17^{+} aberrant basaloid cells along Slingshot-inferred epithelial lineage trajectories. **B** Alveolar-derived trajectory from AT2 to AT1 and aberrant basaloid states. **C** Airway basal cell–derived

trajectory illustrating potential origin of KRT5^{low} and KRT5^{-} cell. **D** Expression dynamics of 12 aberrant basaloid signature genes (*KRT5, KRT17, CDH1, MMP7, SOX4, SOX9, ITGB6, ITGAV, CDKN1A, GDF15, SPINK1, and TM4SF1*) plotted along Slingshot pseudotime across basal, KRT5^{low} basal, and KRT5^{-}/KRT17^{+} aberrant basaloid populations. **E,H** Representative hematoxylin and eosin (H&E) images of IPF lung tissues. **F, I** representative CosMx SMI morphology marker (PanCK) images of IPF tissues **G, J** CosMx spatial maps of cell centroids from adjacent tissue sections corresponding to the regions in E and F, highlighting basal cells, KRT5^{low} basal cells, KRT5^{-}/KRT17^{+} aberrant basaloid cells, and AT2 cells. I Ridge plots showing the minimal distance of epithelial subtypes to basal cells, calculated from CosMx spatial coordinates. A red vertical line at 0 marks the basal cell location. keratin 5 (*KRT5*), keratin 17 (*KRT17*), cadherin 1 (*CDH1*), matrix metalloproteinase 7 (*MMP7*), SRY-box transcription factors 4 and 9 (*SOX4, SOX9*), integrin subunit β6 (*ITGB6*), integrin subunit αV (*ITGAV*), cyclin-dependent kinase inhibitor 1A (*CDKN1A*), growth differentiation factor 15 (*GDF15*), serine peptidase inhibitor Kazal type 1 (*SPINK1*), and transmembrane 4 L six family member 1 (*TM4SF1*).

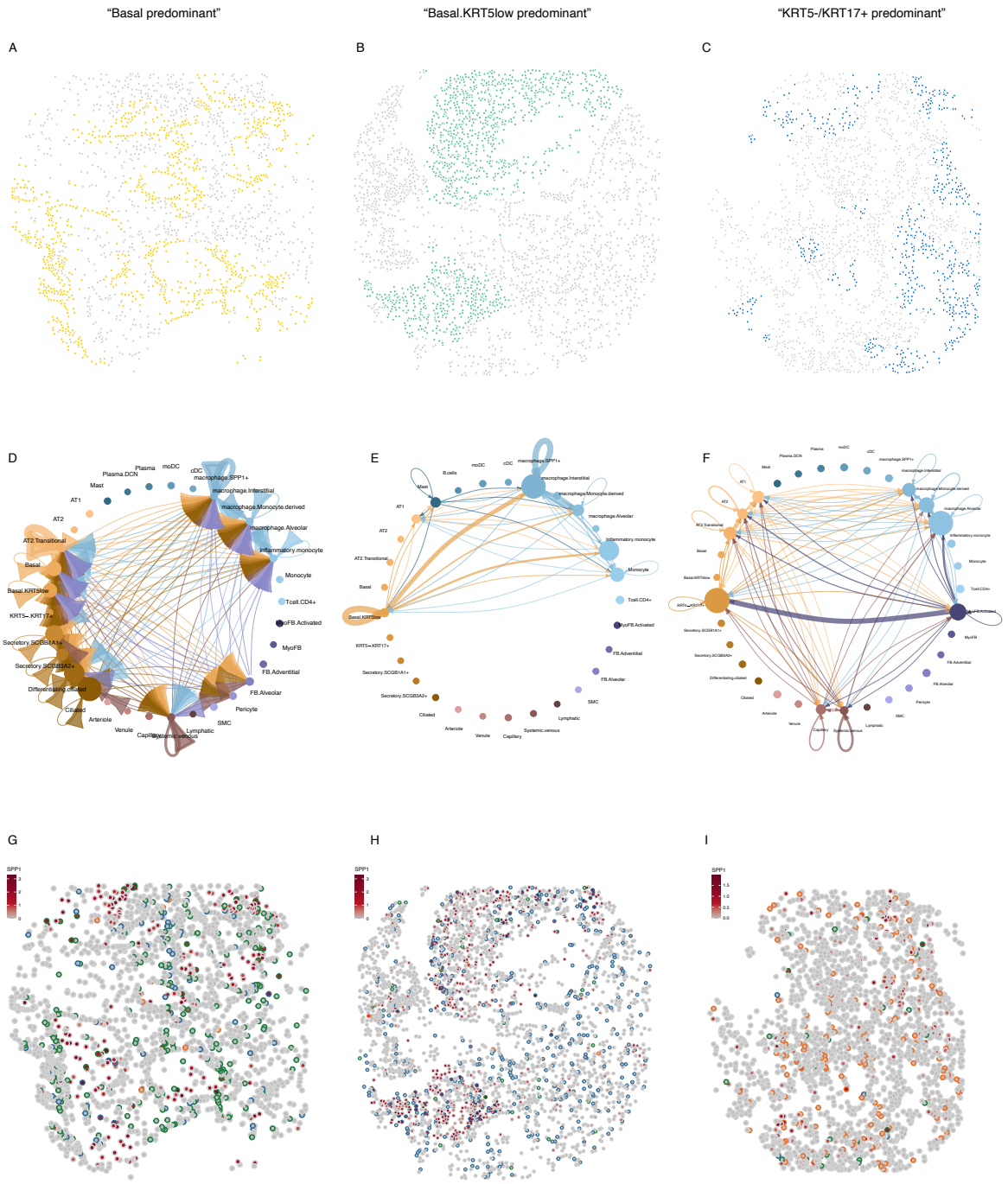

582

583 **Figure 4. Unique epithelial niches orchestrate aberrant cell–cell communication in fibrotic**
584 **lung A–C** Spatial maps of cell centroids highlighting the location of three epithelial niches:
585 basal-predominant (N2, yellow), KRT5^{low} basal–predominant (N7, green), and KRT5^{-}/KRT17^{+}
586 aberrant basaloid–predominant (N3, blue). **D–F** CellChat analysis of inferred ligand–receptor
587 interactions within basal-predominant (D), KRT5^{low} basal–predominant (E), and
588 KRT5^{-}/KRT17^{+}–predominant (F) niches. Nodes represent cell types and edges indicate

589 predicted interactions, with edge width proportional to interaction strength. **G–I** Co-
590 visualization of cell type centroids and SPP1 expression in basal-predominant (G),
591 $KRT5^{-}/KRT17^{+}$–predominant (H), and $KRT5^{low}$ basal–predominant (I) niches. Cell centroid
592 borders are coloured by annotated cell type, and centroid filling is scaled to SPP1 expression
593 levels.

594

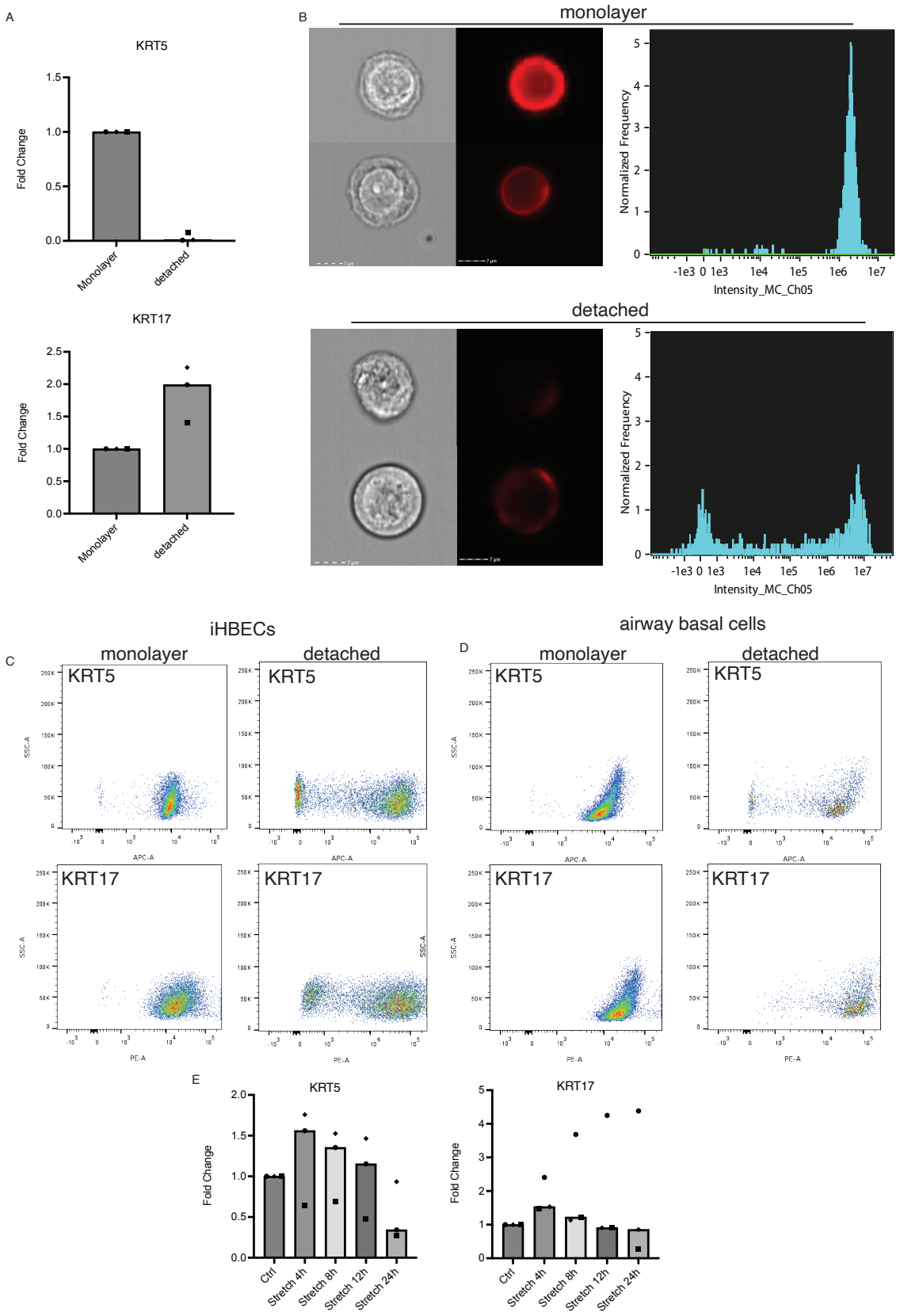

Figure 5 Basal cell detachment is associated with loss of KRT5 expression A ihBECs mRNA Expression of KRT5 and KRT17 (n=3) of monolayer cells and detached cells (collected from supernatant) **B** ihBECs ImageStream MK II Imaging Flow Cytometry of monolayer cells and

599 detached cells (representative data n=2) stained with intracellular KRT5 antibody (2ug/mL). **C**
600 Flow Cytometry using BD FACSCanto of ihBECs monolayer cells and detached cells stained for
601 KRT5 (APC-A) and KRT17 (PE-A) at 2ug/mL (representative data n=3). **D** Flow Cytometry using
602 BD FACSCanto of primary basal monolayer cells and detached cells stained for KRT5 (APC-A)
603 and KRT17 (PE-A) at 2ug/mL (representative data n=2). **E-F** *KRT5* and *KRT17* mRNA expression
604 of small airway epithelial cells (SAECs) subject to cyclic stretch over 24 hours (n=3).

605

606

607

608